ACS APPLIED ENERGY MATERIALS

www.acsaem.org Article

Manganese Porphyrin Interface Engineering in Perovskite Solar Cells

Konstantina Gkini, Nikolaos Balis, Michael Papadakis, Apostolis Verykios, Maria-Christina Skoulikidou, Charalampos Drivas, Stella Kennou, Matthias Golomb, Aron Walsh, Athanassios G. Coutsolelos,* Maria Vasilopoulou,* and Polycarpos Falaras*

Cite This: *ACS Appl. Energy Mater.* 2020, 3, 7353−7363 Read Online

ACCESS | Metrics & More | Article Recommendations | Supporting Information

ABSTRACT: An interfacial engineering approach was adopted in order to optimize the photovoltaic parameters and the stability of n-i-p planar perovskite solar cells (PSCs). A thin manganese (Mn) porphyrin [(TMePyP)I_4Mn(AcO)] layer was introduced between the titania (TiO_2) electron transport layer (ETL) and the perovskite absorber. The introduction of porphyrin onto the TiO_2 substrate provoked a significant decrease in the work function (W_F), which arose from the large local dipole moment. The modification also provided a more hydrophobic environment that favored the growth of homogeneous and large perovskite crystals. Moreover, the electron charge transport to the ETL was facilitated via the highly paramagnetic character of the Mn porphyrin, whereas the negative impact of humidity and oxygen on the PSC performance was hindered. Density functional theory analysis justified the observed large decrease of the W_F and the strong electronic coupling of porphyrin with the TiO_2 compact layer (following the porphyrin deposition), which are beneficial for electron extraction. By combining the Mn porphyrin and the $CH_3NH_3PbI_3$ perovskite, significant enhancement of the stabilized power conversion efficiency by 22% was recorded. The shelf-shield stability was also improved after more than 600 h of storage in the dark under ambient conditions.

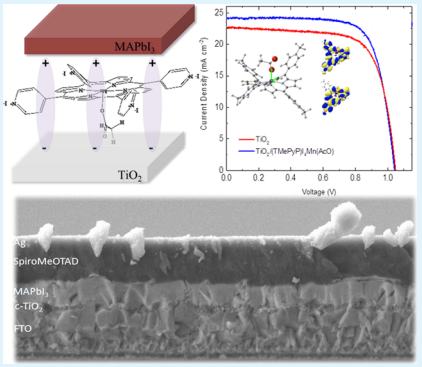

KEYWORDS: *Mn porphyrin, hydrophobic layer, $MAPbI_3$ perovskite, planar PSCs, interface engineering, efficiency and stability increase*

1. INTRODUCTION

Solar energy is one of the most important renewable energy resources, thus research is focused on photovoltaic (PV) devices that can directly convert solar energy into electricity in an effective, eco-friendly, and economical way. Among the third-generation PV technologies, perovskite solar cells (PSCs) have revolutionized the field as they exceeded 25% power conversion efficiency (PCE) within only a few years of development.[1−5] Perovskite absorbers are characterized by near-ideal optoelectronic properties,[6] including the tunable band gap, high carrier mobility,[7] and long carrier lifetime,[8] enabling solution-processed and low-cost fabrication methods.[9]

The state-of-the-art PSCs adopt the mesoporous[10] scaffold configuration, though the planar[11,12] structure is also of interest because of fabrication simplicity and low manufacturing cost. This structure, denoted n-i-p, consists of a perovskite absorber sandwiched between a compact n-type electron transport layer (ETL) and a p-type hole transport layer (HTL). The presence of charge-selective contacts is crucial as they ensure the transport of photogenerated electrons and holes in the perovskite absorber toward the anode and cathode electrodes. In general, their role concerns the optimization of the energy barriers necessary for the selective extraction of the corresponding type of charge carriers and the blocking of the opposite as well as the beneficial alteration of physical contact (*i.e.,* reduced hydrophilicity and a lower surface roughness) between the electrodes and the corresponding photoactive layer.[13] Besides the PCE increase, they also affect the overall stability of PSCs, as these devices can also suffer from intrinsic instability and/or degradation of the perovskite layer under external strain such as UV light, thermal stress, or electric bias.[14]

Therefore, the functionality of ETL and HTL is crucial for the device's overall performance. Concerning the ETL, compact titanium dioxide (TiO_2) is among the best performance materials used in planar PSCs, disposing excellent transmittance and energy bands suitable for a large number of perovskite materials, while it can be easily synthesized and deposited by solution-processed methods.[15] Nevertheless,

Received: March 31, 2020
Accepted: July 21, 2020
Published: July 21, 2020

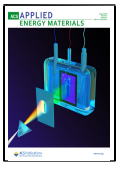

https://dx.doi.org/10.1021/acsaem.0c00710
ACS Appl. Energy Mater. 2020, 3, 7353−7363

TiO_2 is also characterized by low conductivity and poor electron mobility, along with many defects (oxygen vacancies and Ti^{3+} ions) that are responsible for high carrier recombination rates at surface trap states.[16−18] To confront these issues, various modifications of the TiO_2 layer have been proposed including element doping[19,20] or bifacial engineering with other electron transport materials, such as PCBM or SnO_2.[21,22]

In this context, a promising interface engineering approach[23,24] is the incorporation of a dye molecule at the ETL/perovskite interface, which can act as an electron transport mediator and facilitate the electron extraction at the anode. Following this concept, the modification of the TiO_2 ETL by chemisorbing the hydrophobic D35 organic dye[25] resulted in an overall improvement in the PSC device performance and stability attributed to the improved nanomorphology of the photoactive layer and enhanced electron injection rate toward TiO_2. Until now, porphyrins have been widely utilized in various energy-related applications (*i.e.*, organic solar cells, molecular hydrogen production, and so on) because of their unique and easily tunable electrochemical and optical properties.[26−30] In addition, the preparation of symmetrical tetrasubstituted porphyrin macrocycles is a well-established and low-cost approach, thus enabling the large-scale application of such derivatives.[31−34] Zinc (Zn)-metallated porphyrins represent the most studied class of porphyrin materials that have been widely applied as hole transporter interlayers in organic and perovskite hybrid solar cells, respectively.[35−39] As electron transport mediators, they have only been recently introduced in the literature with intriguing results.[40,41] Thus, they comprise robust candidate materials for interfacial engineering.[42,43] We note, however, that until now only zinc-metallated porphyrins have been applied as effective interfacial modifiers despite a vast variety of other metallated porphyrins having been proven to be beneficial in several classes of energy-related applications.[44,45] A notable exception is the recent application of a europium (Eu) porphyrin as a perovskite grain boundary-passivating agent, resulting in the fabrication of PSCs with improved performance and stability.[46] In this work, the authors demonstrated that europium cations may interfere with perovskite crystal formation, hence improving the quality of the resultant perovskite films and reducing the grain boundary-related defect states. Recently, the incorporation of manganese (Mn) cations within the perovskite precursor has shown to have similar effects as it allowed the fabrication of defect-passivated perovskite films and enhanced the performance of the corresponding solar cells.[47]

Herein, we expand the investigation on porphyrin compounds as interfacial materials by incorporating Mn porphyrin in the ETL/perovskite interface of planar PSCs, resulting in a significant increase in the stabilized PV efficiency. We based our selection on the established role of Mn-bearing compounds in controlling the grain size and passivating defects in several types of perovskite materials.[48] We found that the role of the porphyrin interlayer above the TiO_2 substrate is very crucial for the device operation. Indeed, it creates a more hydrophobic environment that favors the growth of more homogeneous and stable perovskite films with larger and better crystallized perovskite grains. This leads to a net increase in the photocurrent density, a fact clearly reflected in the total PCE improvement. Moreover, the porphyrin interlayer improves the electron transfer to the anode through a significant decrease in the work function (W_F) of the ETL combined with suppression in charge recombination. The latter could be related to the passivation effect of Mn in the perovskite absorber in agreement with recent reports, which demonstrated that Mn^{2+} could be easily inserted into the interstices of octahedral $[PbI_6]^{4-}$ to restrain the generation of vacancy defects accompanying perovskite crystallization.[47,48] As a result, we obtained porphyrin-based PSCs enhanced by 22% in terms of stabilized PCE compared to the reference ones, reaching a PCE of 18.70% for the best device. Moreover, the efficiency enhancement was accompanied by a clear stabilization of the PSC, which retained 75% of the initial PCE after 1000 h of storage under dark and relatively dry conditions (RH ∼ 20%). The results on Mn porphyrin together with those obtained with zinc-metallated analogues expand the application field of our approach and further highlight the promising perspectives of metalloporphyrin molecules for interface engineering in perovskite devices.

2. EXPERIMENTAL SECTION

2.1. Synthesis of (TMePyP)I_4Mn(AcO). Free base porphyrin (500 mg) was dissolved in 250 mL of dimethyl formamide (DMF). The solution was heated and sluggishly stirred until complete solubilization of the porphyrin. Then, 10 equiv of Mn(II) acetate [$Mn(AcO)_2$] were added, and the solution was left until boiling. After the reaction, the mixture was cooled down to room temperature and transferred to an ice-cold, saturated solution of sodium chloride. A green precipitate formed, which was rinsed with deionized water and dried under air flow. Finally, it was transferred to a dry aluminum oxide column whereby it was eluted with dichloromethane (CH_2Cl_2) and afterward with a mixture of CH_2Cl_2/methanol (MeOH). Recrystallization from CH_2Cl_2 at 4 °C gave 80−90% yield.[49,50]

2.2. Fabrication of PSCs. Fluorine-doped tin oxide (FTO) conductive substrates (20 mm × 15 mm, Dyesol 7 Ω sq^{-1}) were cleaned thoroughly by sonication in sequential baths with Hellmanex, 2-propanol, and acetone for 15 min each. The FTOs were also treated by UV ozone for 15 min before the compact layer deposition. For the ETL, a solution of titanium(IV) isopropoxide (Aldrich, 97%) in ethanol was spin-coated at 2000 rpm for 60 s. The TiO_2 films were annealed at 500 °C for 45 min with a temperature ramp rate of 5 °C min^{-1}. For the porphyrin-modified films, a 0.5 mg mL^{-1} methanolic solution was spin-coated at 2000 rpm for 40 s on top of the TiO_2 films. The samples were transferred into an argon-filled glovebox, where the $CH_3NH_3PbI_3$ layer was deposited. For the perovskite solution, 40 wt % of methylammonium iodide (Dyesol) and lead acetate trihydrate ($PbAc_2{\cdot}3H_2O$, 99.999% trace metal basis, Aldrich) were diluted in anhydrous DMF in a 3:1 molar ratio. The perovskite solution was completed by adding a small amount of hypophosphorous acid (50% w/w, aqueous solution, Alfa Aesar). The perovskite films were obtained by spin-coating the solution on the ETLs at 2000 rpm for 45 s. The films were then allowed to dry at room temperature for 10 min and afterward annealed at 100 °C for 10 min. After cooling down, a 70 mM Spiro-MeOTAD (Solaronix) solution in chlorobenzene, containing additives of lithium bis(trifluoromethanesulfonyl)imide lithium salt (≥99%, Aldrich) in acetonitrile, 4-*tert*-butylpyridine (96%, Aldrich), and FK209 Co(III) TFSI salt in acetonitrile, was spin-coated at 4000 rpm for 10 s. The devices were completed outside the glovebox by thermally evaporating 100 nm of patterned silver electrodes under a 10^{-6} Torr vacuum at an ∼1 Å s^{-1} rate.

2.3. Characterization Tools. A solar simulator (Solar Light Company, Inc. 300W model 16S-300/1 sun, AM 1.5D, 1000 W m^{-2}) and an Autolab PG-STAT-30 potentiostat were used to illuminate the devices and obtain the current−voltage (J−V) curves (scan rate: 50 mV s^{-1}) and record data for stabilized maximum power point (MPP) conditions. Incident photon-to-current efficiency (IPCE) plots were acquired using a custom-made apparatus consisting of an Oriel monochromator and an Oriel Xe lamp working in combination with cutoff optical filters (AM1.5D, AM0, and 400 nm) and the previously

https://dx.doi.org/10.1021/acsaem.0c00710
ACS Appl. Energy Mater. 2020, 3, 7353−7363

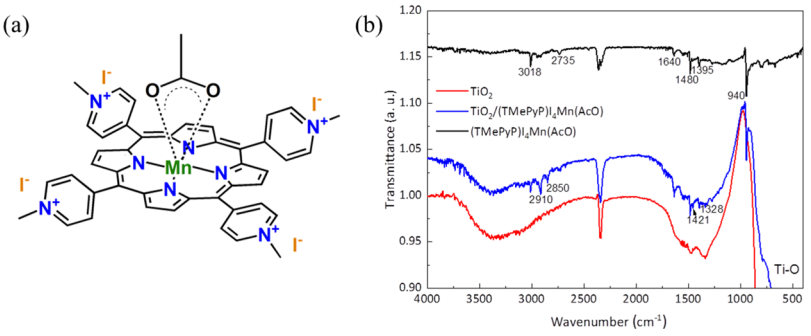

Figure 1. Molecular structure of (TMePyP)I_4Mn(AcO) (a); FTIR spectra of pristine (TMePyP)I_4Mn(AcO), TiO_2, and TiO_2/(TMePyP)I_4Mn(AcO) films on silicon substrates (b).

mentioned potentiostat. Electrochemical impedance spectroscopy (EIS) measurements were also carried out under dark and 1 sun illumination conditions using the PG-STAT-30 potentiostat and its built-in frequency response analyzer. Raman spectroscopy was performed using a Renishaw inVia Reflex microscope with a solid-state Ar laser (λ = 514.4 nm) excitation source. The laser light was focused on the samples using a ×50 objective lens of a Leica DMLM microscope at a power density equal to 0.035 mW μm^{-2} in order to avoid sample heating. X-ray and ultraviolet (UV) photoelectron spectroscopy (XPS and UPS) measurements were carried out for the two samples [reference: TiO_2 and TiO_2/$Mn(AcO)_2$]. The samples were introduced into an ultrahigh vacuum chamber without any prior treatment. XPS measurements were carried out using an unmonochromatized Al Kα line at 1486.6 eV (12 kV with 20 mA anode current) and a Leybold EA-11 analyzer with a constant pass energy of 100 eV, giving a full width at half-maximum (fwhm) of 1.5 eV for the Au $4f_{7/2}$ peak. In all XPS spectra, the binding energy (BE) of the C 1s peak at 284.8 eV was used as a measured BE reference. UPS measurements were carried out using HeI (21.2 eV), the same analyzer, and a constant retarded ratio of 4. Also, a negative bias of 12.22 V was applied between the sample and the analyzer in order to separate the secondary electrons of the analyzer. The UV−vis absorption and transmittance spectra were recorded with a PerkinElmer LAMBDA 40 UV−vis spectrometer. The Fourier-transform infrared (FTIR) spectra were collected with a Bruker Tensor 27 spectrometer. The morphology of the perovskite films was investigated with a field emission scanning electron microscope (JEOL 7401F). X-ray diffraction (XRD) patterns were obtained with a Siemens D500 diffractometer. Photoluminescence (PL) measurements were carried out on a HORIBA Jobin-Yvon iHR320 spectrometer with a He−Cd laser (325 nm) as an excitation source.

2.4. Computational Methods. All electronic structure calculations were done using the FHI-aims package[51] with the nonlocal hybrid HSE06 functional. Standard convergence criteria for electronic (10^{-4} e/Å^3 for the charge density and 10^{-5} eV for the total energy) and relaxation parameters (10^{-2} eV/Å for forces) were applied. All structures were first relaxed with a tier 1 atom-centered basis set, followed by a relaxation in a tighter tier 2 basis. The magnetic ground state was determined to be the Mn(III) high spin. The electric dipole tensor was calculated from the self-consistent electron density. All resulting isodensities were plotted with an isosurface value of 0.025.

3. RESULTS AND DISCUSSION

Figure 1a presents the chemical structure of (TMePyP)I_4Mn-(AcO) porphyrin, hereafter termed (TMePyP)I_4Mn(AcO), while the detailed synthetic route of (TMePyP)I_4Mn(AcO) is presented in Figure S1. The FTIR spectrum of the (TMePyP)I_4Mn(AcO) (Figure 1b) film exhibits the typical bands of pyrrole and phenyl rings.[52,53] The bands at 3018 and 1395 cm^{-1} correspond to CH (pyrrole and phenyl), whereas the bands at 2735 and 1480 correspond to NH (phenyl and pyrrole) stretching. A strong band at 940 cm^{-1} is due to the metalloporphyrin skeletal ring.[54,55] Moreover, the band at 1640 cm^{-1} is due to C═O stretching. These bands are quite distinct in the spectrum of TiO_2 coated by the porphyrin layer, indicating successful anchoring of the metalloporphyrin onto the oxide surface. Furthermore, new bands appear in the spectrum of the porphyrin compound coated on TiO_2. Those centered at 1421 and 1328 cm^{-1} are assigned to C−O stretching, indicating that (TMePyP)I_4Mn(AcO) is chemically attached onto the oxide through the carbonyl group via the formation of C−O−Ti bonds.[56] Such chemical attachment brings porphyrin molecules closer to the ETL, hence strengthening their electronic coupling which is beneficial for charge transfer.

Further evidence for the successful anchoring of porphyrin onto the TiO_2 surface was obtained by XPS. Figure S2 shows the N 1s, I 3d, and C 1s XPS peaks, respectively, detected on TiO_2 coated with (TMePyP)I_4Mn(AcO). Figure S2a shows the XPS spectrum of the N 1s region. Two peaks can be seen, one at 402.4 ± 0.0.2 eV BE and one at 399.9 ± 0.2 eV. The high BE peak is attributed to the N^+ atoms of the porphyrin bonded with I^- ions,[57] whereas the other one corresponds to the N atoms of the porphyrin ring bonded with the Mn atom.[58] In Figure S2b, the XPS spectrum of the I 3d region is shown. The I 3d peak appears as a doublet because of the spin−orbit-splitting (SOS) of the $3d_{5/2}$ and $3d_{3/2}$ components. The $3d_{5/2}$ peak is located at a BE of 617.7 ± 0.2 eV with an SOS of 11.7 ± 0.2 eV for the XPS I 3d peak. In Figure S2c the C 1s XPS spectrum is shown. The adventitious carbon cannot be distinguished from the porphyrin carbon, as they are both sp^2-bonded. Apart from the C−C bonds, other species are present, C−O, C═O, and O−C═O at higher BEs both from the porphyrin molecule and the atmospheric contamination.

The absorption and transmission spectra of the as-deposited and porphyrin-coated TiO_2 (Figures S3 and S4, respectively) confirm that the optical properties of TiO_2 films are not significantly altered upon porphyrin functionalization. In fact, the optical band gap of TiO_2 was estimated at 3.2 eV before and after (TMePyP)I_4Mn(AcO) coverage. Note that the low absorption of manganese porphyrin in the visible region (400−800 nm) (Figure S3) makes it suitable for anode interface engineering in n-i-p PSCs as it does not compete with the perovskite absorber for the incident photons. Particularly, the absorption spectrum of (TMePyP)I_4Mn(AcO) in methanol shows a distinct Soret band at 425 nm and a weak Q-band above 500 nm, representing excitations in the second and first excited states, respectively.[59] Scanning electron microscopy (SEM) images revealed the slight influence of the porphyrin layer on the morphology of the TiO_2 substrate (Figure S5). In

https://dx.doi.org/10.1021/acsaem.0c00710
ACS Appl. Energy Mater. 2020, 3, 7353−7363

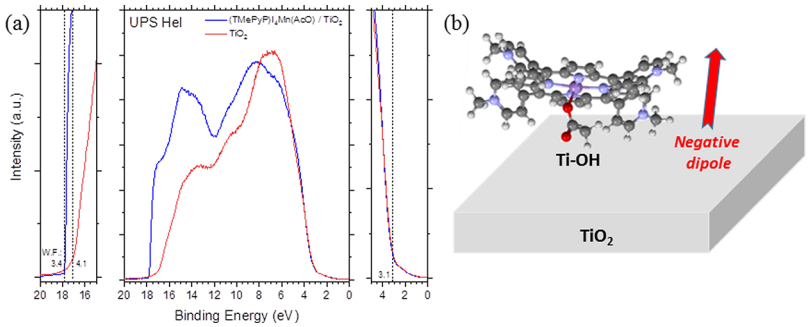

Figure 2. UPS spectra of TiO_2 (on FTO glass) and TiO_2/(TMePyP)I_4Mn(AcO) films: (a) schematic diagram of the interaction between (TMePyP)I_4Mn(AcO) and the TiO_2 substrate and (b) the corresponding dipole moment.

order to further evaluate the alteration in the surface and physical properties of the TiO_2 substrate, we performed contact angle measurements, which showed that (TMePyP)-I_4Mn(AcO) creates a more hydrophobic environment (Figure S6). As is seen, the mean contact angle increases from 25.4 to 56.3° after TiO_2 is coated with porphyrin molecules. This might affect the formation of the perovskite layer as it is well established that nonwetting surfaces create an environment of lower surface tension, associated with less nucleation centers in comparison with the unmodified hydrophilic ones.[60] As a result, larger and more homogeneous perovskite crystals are expected to be formed.

Moreover, changes in the surface electronic properties of TiO_2 upon porphyrin coverage were probed using UPS. Figure 2 illustrates the results of the UPS measurements performed over TiO_2 and (TMePyP)I_4Mn(AcO)/TiO_2 layers coated upon FTO substrates. In the right and left parts of Figure 2a, magnified regions of the valence band (VB) and secondary electron's cutoff, respectively, are presented. With UPS, the W_F is estimated by subtracting the secondary electron cutoff value, based on a linear extrapolation toward the background, from the He excitation source of 21.22 eV (Φ = 21.22 eV − E_{sec}). Additionally, the VBM is determined by a linear extrapolation toward the background in the low BE region, as shown in Figure 2a (right part).

No change is observed at the VB, giving a VB maximum at 3.1 ± 0.1 eV for both samples. Considering the W_F, however, a large decrease by 0.7 ± 0.1 eV is observed after the porphyrin deposition, from 4.1 ± 0.1 eV for the reference sample to 3.4 ± 0.1 eV. This fact proves that (TMePyP)I_4Mn(AcO) anode modification induces a downward vacuum level (VL) shift that modifies the W_F of the anode.[61] Such significant VL shift could be the result of the formation of a large interfacial dipole with the negative pole directed away from the substrate, as illustrated in Figure 2b. This dipole could be related to the interfacial electron transfer from porphyrin molecules to TiO_2 upon chemical binding of porphyrin to the metal oxide substrate through the −C═O anchoring group.[62] As the porphyrin contains a paramagnetic metal (*i.e.*, Mn with atomic number Z = 25) containing five single electrons in 3d valence orbitals, its strong electronic coupling with TiO_2 favors the electron transfer toward the latter. This is supported by the fact that TiO_2 is considered more electronegative compared to porphyrin compounds. It could also be the result of the orientation of porphyrin molecular dipole moment components pointing away from the substrate or a combination of both.[63] A molecular dipole moment pointing away from the substrate denotes that the bulk chemical potential of the electrons is negative relative to the mean electrostatic potential on the metal oxide interior due to charge transfer or by the redistribution of the electron density on the surface. This indicates that less energy is needed for the outer electrons to be spilled out in the VL, which means that the surface W_F decreases. The decrease of 0.7 eV in W_F could be detrimental for the device operation, as it indicates that the Fermi level of the modified TiO_2 lies above the conduction band of the perovskite absorber. However, even if this is the case, the large magnitude and direction of the formed interfacial dipole significantly strengthen the device built-in voltage and sweep electrons away from the perovskite absorber, hence substantially facilitating electron transfer toward the anode. In addition, it has been demonstrated that a significant decrease in the surface W_F of TiO_2 (up to a final value of about 3.0 eV) is generally considered beneficial for the performance of third-generation solar cells because it can suppress or even eliminate the electron extraction barrier.[64,65]

The observations of a large dipolar shift are confirmed in our theoretical calculations based on density functional theory (DFT). Figure 3 shows the porphyrin with Mn(III) in a high-spin configuration after geometry relaxation and its corresponding highest occupied and lowest unoccupied molecular orbitals (HOMO and LUMO, respectively).

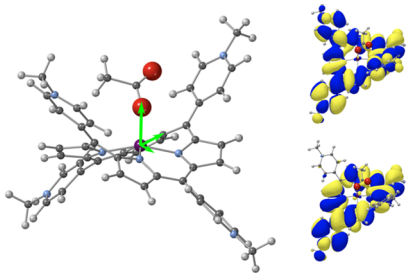

Figure 3. Relaxed Mn porphyrin structure obtained in DFT calculations, with green arrow lengths showing the corresponding dipole moment strength in the corresponding directions (left); HOMO (bottom) and LUMO (top) of the molecule (right).

We can relate the molecular dipole moment to the change in the work function W_F via the Helmholtz equation for describing the potential difference across an electric double layer at a surface[65]

$$\Delta V = \frac{\mu}{\varepsilon_0 A} \quad (1)$$

https://dx.doi.org/10.1021/acsaem.0c00710
ACS Appl. Energy Mater. 2020, 3, 7353−7363

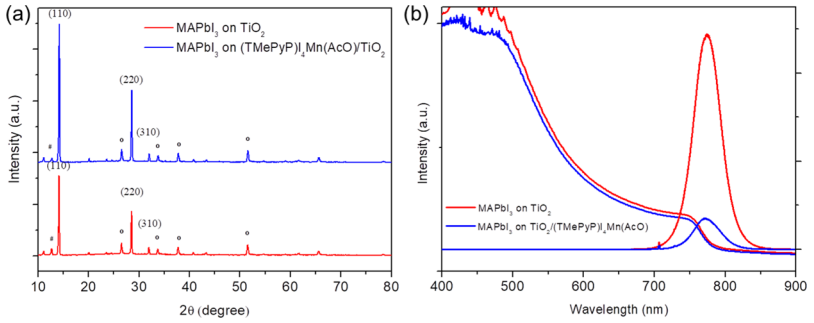

Figure 4. XRD patterns of perovskite films on TiO_2 and TiO_2/(TMePyP)I_4Mn(AcO). Symbols "o", "*", and "#" refer to TiO_2, perovskite, and PbI_2 phases, respectively (a); UV−vis absorption and steady-state PL spectra of perovskite films grown on TiO_2 substrates with and without (TMePyP)I_4Mn(AcO) modification (b).

where μ/A is the dipole moment surface density and ε_0 is the permittivity of free space. Assuming the square planar base of the porphyrin to be the surface, we calculate the out-of-plane dipole moment to be 3.17 Debye, resulting in an upper boundary of 0.69 V for the potential difference based on a fully orientated layer of porphyrins with complete coverage.

Subsequently, XRD measurements were performed in order to evaluate the crystallinity of the perovskite films. As shown in Figure 4a, the absorber deposited on (TMePyP)I_4Mn(AcO)/TiO_2 exhibits higher crystallinity compared to the reference one.

The XRD patterns of both samples contain characteristic diffraction peaks (2θ = 14.15, 28.65, and 32.03°) of crystalline $MAPbI_3$ in agreement with the theoretically expected ones, denoting a well-crystallized perovskite in the tetragonal phase.[66,67] Moreover, a slight difference in the fwhm values (assigned to the 110 peak) for the perovskite is observed between the two patterns, 0.170 for the reference and 0.166 for the modified sample. This difference reflects a higher crystallinity for the perovskite films grown on the TiO_2/(TMePyP)I_4Mn(AcO) substrate and leads to larger perovskite grains, a hypothesis further examined by SEM analysis. In every case, higher crystallinity and larger crystals represent an additional advantage for the device performance as it indicates higher charge-transport rates in the porphyrin-modified device. The UV−vis absorption spectra of perovskite films with the same thicknesses, deposited on TiO_2 and TiO_2/(TMePyP)-I_4Mn(AcO) substrates, were quite similar (Figure 4b). However, this is not the case of the steady-state PL spectra (Figure 4b), where the large reduction of the PL intensity observed on the perovskite film deposited on the porphyrin-functionalized oxide substrate clearly suggests highly improved electron injection rates in agreement with the strong electronic coupling and barrier-free electron extraction discussed above.[33] The latter is clearly attributed to the presence of porphyrin, which facilitates charge extraction to the anode. In addition, the PL quenching in the FTO/TiO_2/perovskite structure, observed after porphyrin modification, suggests that the incorporation of (TMePyP)I_4Mn(AcO) decreases the recombination yield in the perovskite layer, hence highlighting an effective electron−hole separation. Moreover, a slight blue shift of the PL peak (774 nm for the modified PSC against 772 nm for the reference one) implies a trap state passivation at the TiO_2/$MAPbI_3$ interface, which could be related to the beneficial effect of Mn on the overall optoelectronic properties of the perovskite absorber.[68,69]

The topology of both films was examined via SEM (Figure 5). As is clearly shown, the perovskite grown on the pristine

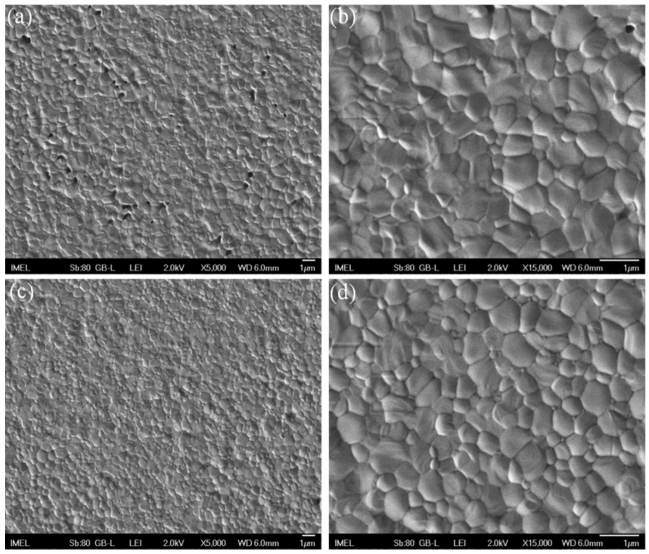

Figure 5. SEM topographies of perovskite films on TiO_2 (a,b) and TiO_2/(TMePyP)I_4Mn(AcO) substrates (c,d).

oxide exhibits obvious pinholes, whereas the perovskite deposited on porphyrin is exempt of pinholes and presents a more homogeneous morphology than the reference. Consequently, the distribution of the grain size is presented in Figure S7. From the data obtained, the mean grain size for the reference sample is 650 nm, while for the modified one the size is larger, about 690 nm. Moreover, the standard deviation of the grain size is larger in the case of the reference sample (0.27 against 0.19 for the modified sample).

This means that more uniform perovskite films are grown on top of the (TMePyP)I_4Mn(AcO)-coated TiO_2, a fact directly related to different degrees of hydrophobicity of the two types of substrates. Interfacial Mn-doping of the perovskite may also occur, which is likely to influence both the lattice and the surface energies of the absorber, as suggested previously.[70−72] Surface passivation during Mn-doping can also lead to stabilization of the perovskite black phase even at room temperature, which is highly beneficial for solar cell performance.

In order to investigate the influence of the porphyrin interlayer on the performance of solar cells, we fabricated PV devices with the following structures: FTO/TiO_2/$MAPbI_3$/

https://dx.doi.org/10.1021/acsaem.0c00710
ACS Appl. Energy Mater. 2020, 3, 7353−7363

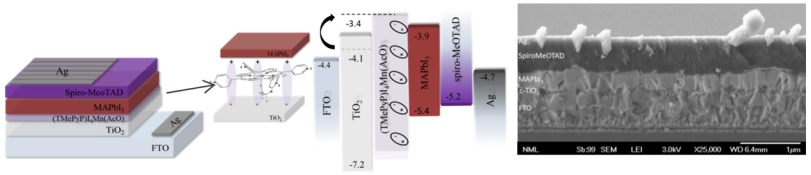

Figure 6. Illustration of the PV device architecture after the insertion of the $(TMePyP)I_4Mn(AcO)$ interlayer (a); energy level diagram of the device (b); and cross-sectional SEM image of a PSC containing the $(TMePyP)I_4Mn(AcO)$ interlayer (c).

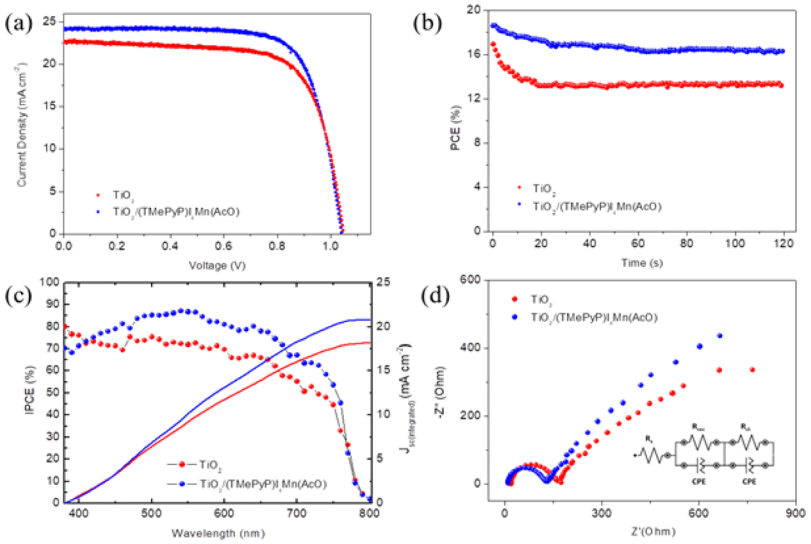

Figure 7. Reverse scan $J-V$ curves (a); steady-state MPP tracking measurements (b); the corresponding IPCE spectra and integration currents (c); and Nyquist plots registered under V_{oc} conditions (d). All curves were recorded for PSCs with the $MAPbI_3$ perovskite absorber grown on pristine (TiO_2) and porphyrin-modified [$TiO_2/(TMePyP)I_4Mn(AcO)$] substrates.

Table 1. Mean Values and Standard Deviation of PV Parameters for Solar Cells Prepared with Bare TiO_2 and $(TMePyP)I_4Mn(AcO)$-Modified TiO_2 ETLs[a]

solar cell	J_{sc} (mA cm^{-2})	V_{oc} (V)	FF	PCE (%)	SPCE (%)
TiO_2	20.40 ± 1.52 (22.62)	1.02 ± 0.03 (1.05)	0.69 ± 0.04 (0.71)	13.92 ± 1.47 (16.94)	13.38
TiO_2/Mn porphyrin	20.94 ± 1.40 (23.52)	1.02 ± 0.02 (1.04)	0.69 ± 0.04 (0.75)	14.10 ± 1.73 (18.70)	16.36

[a]Values inside brackets refer to the most efficient PSCs. V_{oc}: open-circuit voltage, J_{sc}: short-circuit current density, FF: fill factor, PCE: power conversion efficiency, and SPCE: stabilized PCE. All data were taken under a reverse scan at 150 mV s^{-1}

SpiroMeOTAD/Ag as the reference PSC and FTO/TiO_2/$(TMePyP)I_4Mn(AcO)$/$MAPbI_3$/SpiroMeOTAD/Ag as the modified one. Details on the fabrication procedure can be found in the Experimental Section.

Figure 6a depicts the architecture of the perovskite PV devices including the addition of the porphyrin interlayer between TiO_2 and the absorber. Figure 6b illustrates the energy band diagram of the PSCs based on UPS and UV−vis spectroscopy. In Figure 6c, the corresponding cross-sectional SEM image indicates the layered structure of the device with the successive films coated on the FTO substrate. The image, taken at 55° tilt, permits the estimation of the layer thickness of specific cell components as follows: FTO (650 nm), TiO_2/$(TMePyP)I_4Mn(AcO)$ (70 nm), $MAPbI_3$ (330 nm), Spiro-MeOTAD (500 nm), and Ag (100 nm).

Figure 7a presents the $J-V$ curves recorded for the champion devices of each batch under 1 sun illumination conditions (AM 1.5 G) at 150 mV s^{-1} reverse scan rate, while the resulting parameters are summarized in Table 1. From these data, the increase in the PCE observed for the modified PSCs can be attributed to the increase of J_{sc} and FF values. On the other hand, V_{oc} is almost unaffected. Specifically, the short-circuit current density for the champion-modified device is larger by 4% compared to the reference one, reaching a value of 23.52 mA cm^{-2}. This stems from the presence of $(TMePyP)I_4Mn(AcO)$, which is accompanied by a negative dipole moment pointing out of the TiO_2 and facilitating the charge transfer to the anode. Moreover, increased J_{sc} is also associated with the better crystalized, homogenous perovskite films grown on the hydrophobic porphyrin substrate. In the case of fill factor (FF), the modified PSCs have a higher value (0.75) against the reference ones (0.71). This behavior usually implies smoother and more functional interfaces,[73] a fact that may be associated with a change in the values of series and charge transfer resistances for the modified PSCs. Besides the best-performing PSCs, in Figure S8, the PV parameters for 30 devices of each configuration are presented.

The PV behavior of the devices was also evaluated by measuring their efficiency when operating under MPP voltage (V_{MPP}). As depicted in Figure 7b, the stabilized efficiency of the porphyrin-based PSC is 16.36%, a value clearly improved in comparison to the reference device which presents a PCE

https://dx.doi.org/10.1021/acsaem.0c00710
ACS Appl. Energy Mater. 2020, 3, 7353−7363

equal to 13.38%. This difference in favor of the device containing (TMePyP)I_4Mn(AcO) proves the beneficial role of porphyrin in the overall performance of the solar cells. Moreover, IPCE measurements were performed and the integrated current density values were calculated. The IPCE curves (Figure 7c) present a similar trend; however, the modified device shows higher quantum photon to electron conversion efficiencies in the whole visible region, a fact that affects the integrated J_{sc} values. The devices seem to primarily absorb in the visible and IR regions, a fact consistent with the energy band gap of the $MAPbI_3$ absorber. Moreover, the IPCE maximum values are approximately 90% for the modified and 75% for the reference devices, respectively. Finally, the integrated J_{sc} values are in good agreement with those derived from the $J-V$ characteristics, considering the omitted part of the spectrum (UV).

In order to better understand the behavior of the corresponding interfaces, the devices were further investigated by EIS, the details of which are presented in Figure 7d and Table 2. The EIS measurements were performed for solar cells

Table 2. Values of the Ohmic Resistances As Derived from the Simulation of the Nyquist Plots[a]

solar cell	R_s (Ω)	R_{ct} (Ω)	R_{rec} (kΩ)
TiO_2	20.5	131	1.64
TiO_2/(TMePyP)I_4Mn(AcO)	10.7	111	2.39

[a] R_s is the series, R_{ct} is the charge transfer, and R_{rec} is the recombination resistance.

irradiated under 100 mW cm^{-2} illumination, while the cells were biased at a voltage equal to the V_{oc} value. The Nyquist plots were taken while illuminating the solar cells in the 1 MHz to 0.1 Hz range under 10 mV AC perturbation.

The Nyquist plots represent two distinct processes taking place, namely, charge transfer and charge recombination. The high-frequency semicircle is related to the charge-transfer resistance (R_{ct}) and the low frequency one to the charge-recombination resistance (R_{rec}). Moreover, the intercept of the high-frequency arc with the x-axis corresponds to the series resistance (R_s). As the PSCs (except for the porphyrin) are identical, any difference in the corresponding parameters may be attributed to the presence of (TMePyP)I_4Mn(AcO). The ohmic resistance parameters were estimated after fitting the curves under the equivalent circuit presented in the inset of Figure 7d. The presence of porphyrin decreased both series and charge-transfer resistances of the modified PSCs, indicating that the porphyrin facilitates charge transfer to the anode and improves the overall conductivity of the devices. Moreover, the recombination resistance increased in the case of the modified PSC. Lower recombination clearly proves that the presence of porphyrin acts as a protecting barrier, retarding electron transfer back from electrodes to the perovskite layer and suppressing electron loss pathways.

Finally, we performed stability tests for the PSCs, against humidity exposure and thermal stress. At first, devices with and without porphyrin were fabricated and stored under dark and relatively humid conditions (RH ~ 20%) in a sealed desiccator. The $J-V$ curves of the PSCs were recorded before storage, while the samples were periodically taken out of the desiccator in order to get their PV characteristics re-evaluated. The measurements lasted for a 40 day period, and the results are presented in Figure 8. The modified PSCs retained almost 70% of the initial PCE, while the reference one lost approximately three quarters of its efficiency. This trend is mainly attributed to the decline of J_{sc} and FF values. Especially, in the case of J_{sc}, the reference device loses almost 50% of its initial value; on the contrary, the porphyrin-based ones retain 85% of it. Moreover, in the case of FF, after an increase above the initial value, the final value after 43 days is equal to the one that was initially calculated. On the other hand, it must be noticed that V_{oc} is practically unaffected in the case of (TMePyP)I_4Mn(AcO)-containing devices, whereas in the case of the reference ones, it loses 10% of its initial value. Porphyrins are generally compounds of high hydrophobicity. As such, the deposition of Mn porphyrin onto the TiO_2 surface is expected to reduce its well-known hydrophilicity, hence prohibiting the adsorption of water molecules prior to perovskite deposition. As the adsorbed water molecules can act as degradation agents for the

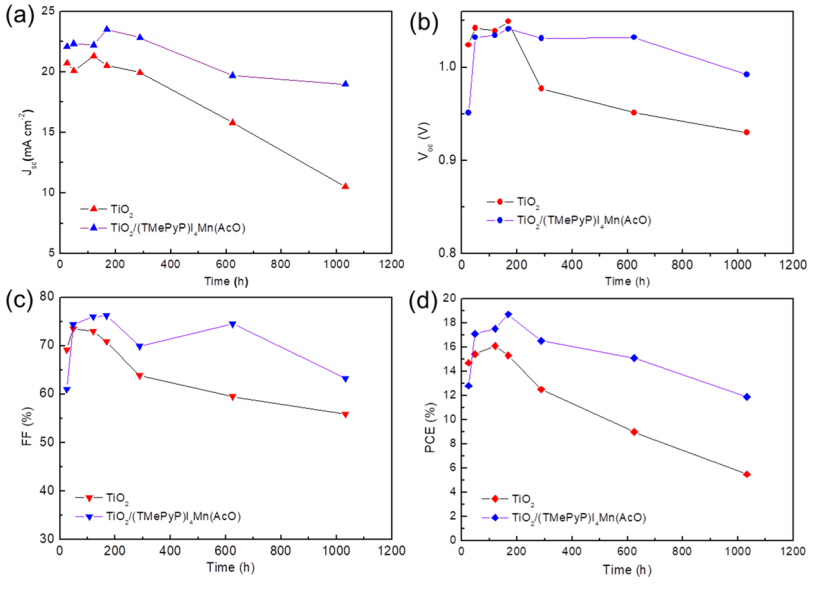

Figure 8. Evolution of the PV parameters over time for PSCs with pristine and porphyrin-modified TiO_2 substrates.

https://dx.doi.org/10.1021/acsaem.0c00710
ACS Appl. Energy Mater. 2020, 3, 7353−7363

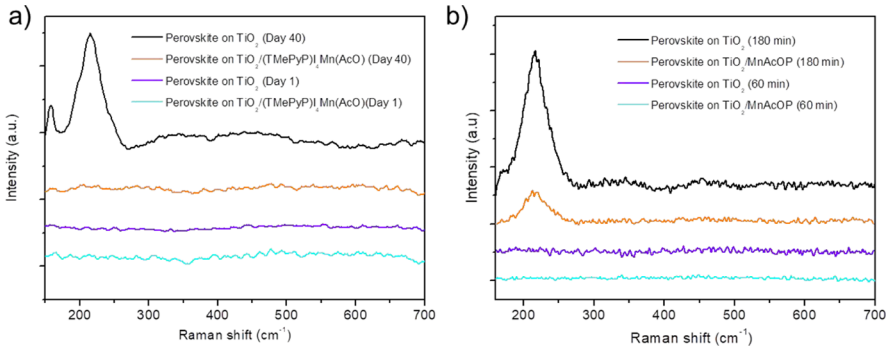

Figure 9. Raman spectra for fresh and aged perovskite layers coated upon TiO_2 and porphyrin/TiO_2 substrates (a). Raman spectra of perovskite layers coated upon TiO_2 and porphyrin/TiO_2 substrates, thermally stressed in air for 60 and 180 min (b).

perovskite absorber, porphyrin modification suppresses the moisture-induced degradation of the final device.

The effect of humidity stress on the perovskite films was further examined via Raman spectroscopy, and the results are shown in Figure 9a. Specifically, the following layered structures were fabricated: FTO/TiO_2/perovskite denoted as the reference one and FTO/TiO_2/(TMePyP)I_4Mn(AcO)/perovskite denoted as the modified one.

As mentioned in ref 74, no Raman signal of the pristine perovskite can be detected under on-resonance Raman excitation because of laser-induced degradation and phase transformations. Thus, only the PbI_2 deterioration products formed on the samples were recorded by Raman spectroscopy. The aging effect was evaluated after the fabricated structures were stored in the dark, inside a desiccator (RH ~ 20%) for 40 days. The reference device deteriorates significantly, as the appearance of the intense vibration peak at 215 cm^{-1} is attributed to the formation of PbI_2.[75,76] On the contrary, the perovskite structures containing porphyrin were not affected. In fact, the obtained spectra did not present any Raman vibration peaks at all, verifying the endurance of these samples against moisture-provoked degradation. This condition was further corroborated by images of films left outside the desiccator under ambient conditions for 100 days (Figure S9). As we can see, the reference sample has turned almost completely yellow, a clear sign of PbI_2 formation. On the contrary, the modified structure remained intact making obvious that the porphyrin layer, as it is hydrophobic, effectively protects the perovskite absorber. To further examine the stabilization effect of the porphyrin, we conducted accelerated thermal stress experiments in perovskite films grown on top of FTO/TiO_2 and FTO/TiO_2/(TMePyP)-I_4Mn(AcO) substrates. As moisture and oxygen penetration may be restricted via the encapsulation of the PSCs,[77] their performance during high-operating temperatures constitutes a very important issue toward large-scale applications.[78,79] Solar cells should be stable when operating at 85 °C which, according to the International Standard for design qualification and type approval of PVs (IEC 61646), is the value that corresponds to the highest expected temperatures that PV modules may develop when the air temperature reaches 45 °C.[80] According to the literature, $CH_3NH_3PbI_3$ alone is stable up to 300 °C, and the material degrades only above this temperature because of the decomposition of the $CH_3NH_3^+$ component.[81] In this context, the films were heated at 85 °C under ambient conditions and evaluated via Raman spectroscopy after 60 and 180 min of thermal treatment. The results are presented in Figure 9b, where it is apparent that after 3 h both samples are affected as the appearance of the PbI_2 peak at 215 cm^{-1} is a clear sign of deterioration. However, even in this case, the porphyrin-based sample outperforms in stability, as the PbI_2 peak is substantially more intense in the case of the reference structure.

4. CONCLUSIONS

In this work, we presented the beneficial effect of a Mn-metallated porphyrin when inserted in planar PSCs as an anode buffer interlayer. The porphyrin molecules are anchored via carbonyl groups upon the TiO_2 substrate, altering its electronic and physical properties, thus creating a waterproof environment. Thus, the perovskite grown atop is characterized by higher crystallinity and larger, more homogeneous crystals. Moreover, the presence of (TMePyP)I_4Mn(AcO) is accompanied by the formation of a strong negative interfacial dipole moment pointing away from TiO_2, resulting in a significant decrease in the W_F of TiO_2. This fact leads to the formation of an optimized interface between the perovskite and TiO_2, thus facilitating electron transport to the anode electrode. The latter is favored by the high-spin pa configuration of the porphyrin, enabling high electron coupling with the TiO_2 underlayer. Moreover, the hydrophobic character of the porphyrin shields the cells against humidity and substantially improves their shelf-shield stability. Excellent behavior was also observed after prolonged thermal stress at high temperatures, a fact highlighting the multidimensional role of (TMePyP)I_4Mn-(AcO) in the overall performance of the devices. The present work highlights the advantages of interface engineering via Mn porphyrin light-sensitive molecular chromophores as a totally aspiring and innovative approach with multiple consequences in the field of PSCs. The strategy can be expanded to a large number of hydrophobic metalloporphyrins possessing appropriate optoelectronic and structural characteristics. Mn molecular complexes show exceptional properties which can be further tuned and optimized via additional magnetic stimulus. This might result in specific interactions at the corresponding interfaces between the compact layer, the magnetic chromophore, and the perovskite absorber, enabling the development of highly efficient and more robust energy devices (solar cells, LEDs, FETs, etc.) against environmental stresses.

https://dx.doi.org/10.1021/acsaem.0c00710
ACS Appl. Energy Mater. 2020, 3, 7353−7363

■ ASSOCIATED CONTENT

Supporting Information

The Supporting Information is available free of charge at https://pubs.acs.org/doi/10.1021/acsaem.0c00710.

Data about the synthetic procedure for the preparation of (TMePyP)I_4Mn(AcO), SEM images, XPS and UV−vis spectra, contact angle images, J−V curves, statistical grain size analysis, and optical images of perovskite films (PDF)

■ AUTHOR INFORMATION

Corresponding Authors

Athanassios G. Coutsolelos − *Department of Chemistry, Laboratory of Bioinorganic Chemistry, University of Crete, Heraklion, Crete 70013, Greece;* orcid.org/0000-0001-5682-2968; Email: coutsole@chemistry.uoc.gr

Maria Vasilopoulou − *Institute of Nanoscience and Nanotechnology, National Center for Scientific Research Demokritos, Athens 15310, Greece;* orcid.org/0000-0001-8893-1691; Email: m.vasilopoulou@inn.demokritos.gr

Polycarpos Falaras − *Institute of Nanoscience and Nanotechnology, National Center for Scientific Research Demokritos, Athens 15310, Greece;* orcid.org/0000-0002-9553-5301; Email: p.falaras@inn.demokritos.gr

Authors

Konstantina Gkini − *Institute of Nanoscience and Nanotechnology, National Center for Scientific Research Demokritos, Athens 15310, Greece*

Nikolaos Balis − *Institute of Nanoscience and Nanotechnology, National Center for Scientific Research Demokritos, Athens 15310, Greece*

Michael Papadakis − *Department of Chemistry, Laboratory of Bioinorganic Chemistry, University of Crete, Heraklion, Crete 70013, Greece*

Apostolis Verykios − *Institute of Nanoscience and Nanotechnology, National Center for Scientific Research Demokritos, Athens 15310, Greece*

Maria-Christina Skoulikidou − *Institute of Nanoscience and Nanotechnology, National Center for Scientific Research Demokritos, Athens 15310, Greece*

Charalampos Drivas − *Department of Chemical Engineering, University of Patras, Rio 26504, Greece*

Stella Kennou − *Department of Chemical Engineering, University of Patras, Rio 26504, Greece*

Matthias Golomb − *Department of Materials, Imperial College London, London SW7 2AZ, U.K.*

Aron Walsh − *Department of Materials, Imperial College London, London SW7 2AZ, U.K.; Department of Materials Science and Engineering, Yonsei University, Seoul 03722, Korea;* orcid.org/0000-0001-5460-7033

Complete contact information is available at: https://pubs.acs.org/10.1021/acsaem.0c00710

Notes

The authors declare no competing financial interest.

■ ACKNOWLEDGMENTS

This work was supported by European Union's Horizon 2020 Marie Curie Innovative Training Network 764787 "MAESTRO" project.

■ REFERENCES

(1) Kojima, A.; Teshima, K.; Shirai, Y.; Miyasaka, T. Organometal Halide Perovskites as Visible-Light Sensitizers for Photovoltaic Cells. *J. Am. Chem. Soc.* **2009**, *131*, 6050−6051.

(2) Liu, M.; Johnston, M. B.; Snaith, H. J. Efficient Planar Heterojunction Perovskite Solar Cells by Vapour Deposition. *Nature* **2013**, *501*, 395−398.

(3) Vasilopoulou, M.; Fakharuddin, A.; Coutsolelos, A. G.; Falaras, P.; Argitis, P.; Yusoff, A. R. b. M.; Nazeeruddin, M. K. Molecular Materials as Interfacial Layers and Additives in Perovskite Solar Cells. *Chem. Soc. Rev.* **2020**, *49*, 4496−4526.

(4) Kim, H. S.; Lee, C. R.; Im, J. H.; Lee, K. B.; Moehl, T.; Marchioro, A.; Moon, S. J.; Humphry-Baker, R.; Yum, J. H.; Moser, J. E.; Grätzel, M.; Park, N. G. Lead Iodide Perovskite Sensitized All-Solid-State Submicron Thin Film Mesoscopic Solar Cell with Efficiency Exceeding 9%. *Sci. Rep.* **2012**, *2*, 591.

(5) Best Research-Cell Efficiency Chart, NREL. https://www.nrel.gov/pv/cell-efficiency.html (accessed October 2019).

(6) Maes, J.; Balcaen, L.; Drijvers, E.; Zhao, Q.; De Roo, J.; Vantomme, A.; Vanhaecke, F.; Geiregat, P.; Hens, Z. Light Absorption Coefficient of $CsPbBr_3$ Perovskite Nanocrystals. *J. Phys. Chem. Lett.* **2018**, *9*, 3093−3097.

(7) Stoumpos, C. C.; Malliakas, C. D.; Kanatzidis, M. G. Semiconducting Tin and Lead Iodide Perovskites with Organic Cations: Phase Transitions, High Mobilities, and Near-Infrared Photoluminescent Properties. *Inorg. Chem.* **2013**, *52*, 9019−9038.

(8) Stranks, S. D.; Eperon, G. E.; Grancini, G.; Menelaou, C.; Alcocer, M. J. P.; Leijtens, T.; Herz, L. M.; Petrozza, A.; Snaith, H. J. Electron-Hole Diffusion Lengths Exceeding 1 Micrometer in an Organometal Trihalide Perovskite Absorber. *Science* **2013**, *342*, 341−344.

(9) Jung, H. S.; Han, G. S.; Park, N.-G.; Ko, M. J. Flexible Perovskite Solar Cells. *Joule* **2019**, *3*, 1850−1880.

(10) Seo, J.-Y.; Uchida, R.; Kim, H.-S.; Saygili, Y.; Luo, J.; Moore, C.; Kerrod, J.; Wagstaff, A.; Eklund, M.; McIntyre, R.; Pellet, N.; Zakeeruddin, S. M.; Hagfeldt, A.; Grätzel, M. Boosting the Efficiency of Perovskite Solar Cells with CsBr-Modified Mesoporous TiO_2 Beads as Electron-Selective Contact. *Adv. Funct. Mater.* **2018**, *28*, 1705763.

(11) Balis, N.; Zaky, A. A.; Athanasekou, C.; Silva, A. M.; Sakellis, E.; Vasilopoulou, M.; Stergiopoulos, T.; Kontos, A. G.; Falaras, P. Investigating the Role of Reduced Graphene Oxide as a Universal Additive in Planar Perovskite Solar Cells. *J. Photochem. Photobiol., A* **2020**, *386*, 112141.

(12) Zhang, X.; Shi, Z.; Lu, H.; Li, X.; Wang, H.; Yuan, S.; Liu, F.; Pan, Y.; Weng, Z.; Zhang, H.; Cui, X.; Liu, Q.; Li, C.; Umar, A. A.; Wang, J.; Hang, X.-C.; Sun, Z.; Zhan, Y. Highly Efficient Planar Perovskite Solar Cells via Acid-Assisted Surface Passivation. *J. Mater. Chem. A* **2019**, *7*, 22323−22331.

(13) Kim, H.; Lim, K.-G.; Lee, T.-W. Planar Heterojunction Organometal Halide Perovskite Solar Cells: Roles of Interfacial Layers. *Energy Environ. Sci.* **2016**, *9*, 12−30.

(14) Roose, B.; Wang, Q.; Abate, A. The Role of Charge Selective Contacts in Perovskite Solar Cell Stability. *Adv. Energy Mater.* **2019**, *9*, 1803140.

(15) Karunakaran, S. K.; Arumugam, G. M.; Yang, W.; Ge, S.; Khan, S. N.; Lin, X.; Yang, G. Recent Progress in Inkjet-Printed Solar Cells. *J. Mater. Chem. A* **2019**, *7*, 13873−13902.

(16) Giordano, F.; Abate, A.; Baena, J. P. C.; Saliba, M.; Matsui, T.; Im, H. S.; Zakeeruddin, S. S. M.; Nazeeruddin, M. K.; Hagfeldt, A.; Grätzel, M. Enhanced Electronic Properties in Mesoporous TiO_2 via Lithium Doping for High-Efficiency Perovskite Solar Cells. *Nat. Commun.* **2016**, *7*, 10379.

(17) Zhu, Z.; Ma, J.; Wang, Z.; Mu, C.; Fan, Z.; Du, L.; Bai, Y.; Fan, L.; Yan, H.; Phillips, D. L.; Yang, S. Efficiency Enhancement of Perovskite Solar Cells Through Fast Electron Extraction: The Role of Graphene Quantum Dots. *J. Am. Chem. Soc.* **2014**, *136*, 3760−3763.

(18) Ho, Y.-C.; Hoque, M. N. F.; Stoneham, E.; Warzywoda, J.; Dallas, T.; Fan, Z. Reduction of Oxygen Vacancy Related Traps in

TiO_2 and the Impacts on Hybrid Perovskite Solar Cells. *J. Phys. Chem. C* **2017**, *121*, 23939−23946.
(19) Liu, D.; Li, S.; Zhang, P.; Wang, Y.; Zhang, R.; Sarvari, H.; Wang, F.; Wu, J.; Wang, Z.; Chen, Z. D. Efficient Planar Heterojunction Perovskite Solar Cells with Li-doped Compact TiO_2 Layer. *Nano Energy* **2017**, *31*, 462−468.
(20) Roose, B.; Gödel, K. C.; Pathak, S.; Sadhanala, A.; Baena, J. P. C.; Wilts, B. D.; Snaith, H. J.; Wiesner, U.; Grätzel, M.; Steiner, U.; Abate, A. Enhanced Efficiency and Stability of Perovskite Solar Cells Through Nd-Doping of Mesostructured TiO_2. *Adv. Energy Mater.* **2016**, *6*, 1501868.
(21) Tavakoli, M. M.; Saliba, M.; Yadav, P.; Holzhey, P.; Hagfeldt, A.; Zakeeruddin, S. M.; Grätzel, M. Synergistic Crystal and Interface Engineering for Efficient and Stable Perovskite Photovoltaics. *Adv. Energy Mater.* **2018**, *9*, 1802646.
(22) Ma, J.; Chang, J.; Lin, Z.; Guo, X.; Zhou, L.; Liu, Z.; Xi, H.; Chen, D.; Zhang, C.; Hao, Y. Elucidating the Roles of TiCl4 and PCBM Fullerene Treatment on TiO2 Electron Transporting Layer for Highly Efficient Planar Perovskite Solar Cells. *J. Phys. Chem. C* **2018**, *122*, 1044−1053.
(23) Zhou, H.; Chen, Q.; Li, G.; Luo, S.; Song, T.-B.; Duan, H.-S.; Hong, Z.; You, J.; Liu, Y.; Yang, Y. Interface Engineering of Highly Efficient Perovskite Solar Cells. *Science* **2014**, *345*, 542−546.
(24) Yang, G.; Wang, C.; Lei, H.; Zheng, X.; Qin, P.; Xiong, L.; Zhao, X.; Yan, Y.; Fang, G. Interface Engineering in Planar Perovskite Solar Cells: Energy Level Alignment, Perovskite Morphology Control and High-Performance Achievement. *J. Mater. Chem. A* **2017**, *5*, 1658−1666.
(25) Balis, N.; Zaky, A. A.; Perganti, D.; Kaltzoglou, A.; Sygellou, L.; Katsaros, F.; Stergiopoulos, T.; Kontos, A. G.; Falaras, P. Dye Sensitization of Titania Compact Layer for Efficient and Stable Perovskite Solar Cells. *ACS Appl. Energy Mater.* **2018**, *1*, 6161−6171.
(26) Charalambidis, G.; Georgilis, E.; Panda, M. K.; Anson, C. E.; Powell, A. K.; Doyle, S.; Moss, D.; Jochum, T.; Horton, P. N.; Coles, S. J.; Linares, M.; Beljonne, D.; Naubron, J.-V.; Conradt, J.; Kalt, H.; Mitraki, A.; Coutsolelos, A. G.; Balaban, T. S. A Switchable Self-Assembling and Disassembling Chiral System based on a Porphyrin-Substituted Phenylalanine-Phenylalanine Motif. *Nat. Commun.* **2016**, *7*, 12657.
(27) Lazarides, T.; Delor, M.; Sazanovich, I. V.; McCormick, T. M.; Georgakaki, I.; Charalambidis, G.; Weinstein, J. A.; Coutsolelos, A. G. Photocatalytic Hydrogen Production from a Noble Metal Free System based on a Water Soluble Porphyrin Derivative and a Cobaloxime Catalyst. *Chem. Commun.* **2014**, *50*, 521−523.
(28) Mikroyannidis, J. A.; Charalambidis, G.; Coutsolelos, A. G.; Balraju, P.; Sharma, G. D. Novel Zinc Porphyrin with Phenylenevinylene Meso-Substituents: Synthesis and Application in Dye-Sensitized Solar Cells. *J. Power Sources* **2011**, *196*, 6622−6628.
(29) Stangel, C.; Daphnomili, D.; Lazarides, T.; Drev, M.; Krašovec, U. O.; Coutsolelos, A. G. Noble Metal Porphyrin Derivatives Bearing Carboxylic Groups: Synthesis, Characterization and Photophysical Study. *Polyhedron* **2013**, *52*, 1016−1023.
(30) Tountas, M.; Verykios, A.; Polydorou, E.; Kaltzoglou, A.; Soultati, A.; Balis, N.; Angaridis, P. A.; Papadakis, M.; Nikolaou, V.; Auras, F.; Palilis, L. C.; Tsikritzis, D.; Evangelou, E. K.; Gardelis, S.; Koutsoureli, M.; Papaioannou, G.; Petsalakis, I. D.; Kennou, S.; Davazoglou, D.; Argitis, P.; Falaras, P.; Coutsolelos, A. G.; Vasilopoulou, M. Engineering of Porphyrin Molecules for Use as Effective Cathode Interfacial Modifiers in Organic Solar Cells of Enhanced Efficiency and Stability. *ACS Appl. Mater. Interfaces* **2018**, *10*, 20728−20739.
(31) Stangel, C.; Bagaki, A.; Angaridis, P. A.; Charalambidis, G.; Sharma, G. D.; Coutsolelos, A. G. "Spider"-shaped Porphyrins with Conjugated Pyridyl Anchoring Groups as Efficient Sensitizers for Dye-Sensitized Solar Cells. *Inorg. Chem.* **2014**, *53*, 11871−11881.
(32) Weber, K. T.; Karikis, K.; Weber, M. D.; Coto, P. B.; Charisiadis, A.; Charitaki, D.; Charalambidis, G.; Angaridis, P.; Coutsolelos, A. G.; Costa, R. D. Cunning Metal Core: Efficiency/Stability Dilemma in Metallated Porphyrin Based Light-Emitting Electrochemical Cells. *Dalton Trans.* **2016**, *45*, 13284−13288.
(33) Zervaki, G. E.; Papastamatakis, E.; Angaridis, P. A.; Nikolaou, V.; Singh, M.; Kurchania, R.; Kitsopoulos, T. N.; Sharma, G. D.; Coutsolelos, A. G. A Propeller-Shaped, Triazine-Linked Porphyrin Triad as Efficient Sensitizer for Dye-Sensitized Solar Cells. *Eur. J. Inorg. Chem.* **2014**, 1020−1033.
(34) Charisiadis, A.; Bagaki, A.; Fresta, E.; Weber, K. T.; Charalambidis, G.; Stangel, C.; Hatzidimitriou, A. G.; Angaridis, P. A.; Coutsolelos, A. G.; Costa, R. D. Peripheral Substitution of Tetraphenyl Porphyrins: Fine-Tuning Self-Assembly for Enhanced Electroluminescence. *ChemPlusChem* **2018**, *83*, 254−265.
(35) Reddy, G.; Katakam, R.; Devulapally, K.; Jones, L. A.; Gaspera, E.; Della Gaspera, H. M.; Islavath, N.; Giribabu, L. Ambient Stable, Hydrophobic, Electrically Conductive Porphyrin Hole-Extracting Materials for Printable Perovskite Solar Cells. *J. Mater. Chem. C* **2019**, *7*, 4702−4708.
(36) Azmi, R.; Lee, U.-H.; Wibowo, F. T. A.; Eom, S. H.; Yoon, S. C.; Jang, S.-Y.; Jung, I. H. Performance Improvement in Low-Temperature-Processed Perovskite Solar Cells by Molecular Engineering of Porphyrin-Based Hole Transport Materials. *ACS Appl. Mater. Interfaces* **2018**, *10*, 35404−35410.
(37) Lv, X.; Xiao, G.; Feng, X.; Cao, J.; Yao, X.; Liu, J. Acylhydrazone-based Porphyrin Derivative as Hole Transport Material for Efficient and Thermally Stable Perovskite Solar Cells. *Dyes Pigm.* **2019**, *160*, 957−961.
(38) Chiang, Y.-H.; Chou, H.-H.; Cheng, W.-T.; Li, Y.-R.; Yeh, C.-Y.; Chen, P. Porphyrin Dimers as Hole-Transporting Layers for High-Efficiency and Stable Perovskite Solar Cells. *ACS Energy Lett.* **2018**, *3*, 1620−1626.
(39) Wu, P.; Zhu, R.; Liu, H.; Zhao, B.; Chen, Y.; Li, X. Surface Decorating of $CH_3NH_3PbBr_3$ Nanoparticles with Chemically Adsorbed Porphyrin. *Colloid Polym. Sci.* **2019**, *297*, 595−601.
(40) Balis, N.; Verykios, A.; Soultati, A.; Constantoudis, V.; Papadakis, M.; Kournoutas, F.; Drivas, C.; Skoulikidou, M.-C.; Gardelis, S.; Fakis, M.; Kennou, S.; Kontos, A. G.; Coutsolelos, A. G.; Falaras, P.; Vasilopoulou, M. Triazine-Substituted Zinc Porphyrin as an Electron Transport Interfacial Material for Efficiency Enhancement and Degradation Retardation in Planar Perovskite Solar Cells. *ACS Appl. Energy Mater.* **2018**, *1*, 3216−3229.
(41) Gkini, K.; Verykios, A.; Balis, N.; Kaltzoglou, A.; Papadakis, M.; Adamis, K. S.; Armadorou, K.-K.; Soultati, A.; Drivas, C.; Gardelis, S.; Petsalakis, I. D.; Palilis, L. C.; Fakharuddin, A.; Haider, M. I.; Bao, X.; Kennou, S.; Argitis, P.; Schmidt-Mende, L.; Coutsolelos, A. G.; Falaras, P.; Vasilopoulou, M. Enhanced Organic and Perovskite Solar Cell Performance through Modification of the Electron-Selective Contact with a Bodipy−Porphyrin Dyad. *ACS Appl. Mater. Interfaces* **2020**, *12*, 1120−1131.
(42) Urbani, M.; De la Torre, G.; Nazeeruddin, M. K.; Torres, T. Phthalocyanines and Porphyrinoid Analogues as Hole- and Electron-Transporting Materials for Perovskite Solar Cells. *Chem. Soc. Rev.* **2019**, *48*, 2738−2766.
(43) Cao, J.; Lv, X.; Zhang, P.; Chuong, T. T.; Wu, B.; Feng, X.; Shan, C.; Liu, J.; Tang, Y. Plant Sunscreen and Co (II)/(III) Porphyrins for UV-Resistant and Thermally Stable Perovskite Solar Cells: From Natural to Artificial. *Adv. Mater.* **2018**, *30*, 1800568.
(44) Wang, L.; Jin, P.; Huang, J.; She, H.; Wang, Q. Integration of Copper (II)-Porphyrin Zirconium Metal-Organic Framework and Titanium Dioxide to Construct Z-Scheme System for Highly Improved Photocatalytic CO_2 Reduction. *ACS Sustainable Chem. Eng.* **2019**, *7*, 15660−15670.
(45) Li, X.; Zhang, Y.; Wang, W.; Meng, J.; Li, K.; Lin, W.; Peng, Z.; Wan, J.; Hu, Z. Fabrication of 1D Long Chain-Like Metal Porphyrin-Based Coordination Complexes for High-Efficiency Hydrogen Evolution and Photoelectric Response. *Int. J. Hydrogen Energy* **2019**, *44*, 18072−18082.
(46) Feng, X.; Chen, R.; Nan, Z.-A.; Lv, X.; Meng, R.; Cao, J.; Tang, Y. Perfection of Perovskite Grain Boundary Passivation by Eu-

https://dx.doi.org/10.1021/acsaem.0c00710
ACS Appl. Energy Mater. 2020, 3, 7353−7363

Porphyrin Complex for Overall-Stable Perovskite Solar Cells. *Adv. Sci.* **2019**, *6*, 1802040.
(47) Liang, J.; Liu, Z.; Qiu, L.; Hawash, Z.; Meng, L.; Wu, Z.; Jiang, Y.; Ono, L. K.; Qi, Y. Enhancing Optical, Electronic, Crystalline, and Morphological Properties of Cesium Lead Halide by Mn Substitution for High-Stability All-Inorganic Perovskite Solar Cells with Carbon Electrodes. *Adv. Energy Mater.* **2018**, *8*, 1800504.
(48) Liu, W.; Chu, L.; Liu, N.; Ma, Y.; Hu, R.; Weng, Y.; Li, H.; Zhang, J.; Li, X. a.; Huang, W. Efficient Perovskite Solar Cells Fabricated by Manganese Cations Incorporated in Hybrid Perovskites. *J. Mater. Chem. C* **2019**, *7*, 11943−11952.
(49) Jiang, X.; Gros, C. P.; Chang, Y.; Desbois, N.; Zeng, L.; Cui, Y.; Kadish, K. M. Tetracationic and Tetraanionic Manganese Porphyrins: Electrochemical and Spectroelectrochemical Characterization. *Inorg. Chem.* **2017**, *56*, 8045−8057.
(50) Tornaritis, M. J.; Coutsolelos, A. G. Metalloporphyrins Catalyse Cis-polybutadiene to Polyepoxide. *Polymer* **1992**, *33*, 1771−1772.
(51) Blum, V.; Gehrke, R.; Hanke, F.; Havu, P.; Havu, V.; Ren, X.; Reuter, K.; Scheffler, M. Ab Initio Molecular Simulations with Numeric Atom-Centered Orbitals. *Comput. Phys. Commun.* **2009**, *180*, 2175−2196.
(52) Nakamoto, K. *Infrared and Raman Spectra of Inorganic and Coordination Compounds, Part A: Theory and Applications in Inorganic Chemistry*, 5th ed.; John Wiley & Sons Inc.: New York, 1997.
(53) Bandgar, B. P.; Gujarathi, P. B. Synthesis and Characterization of New Meso-Substituted Unsymmetrical Metalloporphyrins. *Chem. Sci.* **2008**, *120*, 259−266.
(54) Alston, K.; Storm, C. B. Copper (II) Protoporphyrin IX as a Reporter Group for the Heme Environment in Myoglobin. *Biochemistry* **1979**, *18*, 4292−4300.
(55) Castro, K. A. D. F.; Silva, S.; Pereira, P. M. R.; Simões, M. M. Q.; da Graça, M.; Neves, P. M. S.; Cavaleiro, J. A. S.; Wypych, F.; Tomé, J. P. C.; Nakagaki, S.; Nakagaki, S. Galactodendritic Porphyrinic Conjugates as New Biomimetic Catalysts for Oxidation Reactions. *Inorg. Chem.* **2015**, *54*, 4382−4393.
(56) Zhang, L.; Cole, J. M. Anchoring Groups for Dye-Sensitized Solar Cells. *ACS Appl. Mater. Interfaces* **2015**, *7*, 3427−3455.
(57) Lindberg, B. J.; Hedman, J. Molecular spectroscopy by means of ESCA, VI. Group shifts for N, P and as compounds. *Chem. Scr.* **1975**, *7*, 155.
(58) Canesson, P.; Cruz, M. I.; Van Damme, H. XPS Study of the Interaction of Some Porphyrins and Metalloporphyrins with Montmorillonite. *Dev. Sedimentol.* **1979**, *27*, 217−225.
(59) Ramakrishna, G.; Verma, S.; Jose, D. A.; Kumar, D. K.; Das, A.; Palit, D. K.; Ghosh, H. N. Interfacial Electron Transfer between Photo-excited Porphyrin molecule and TiO_2 Nanoparticles: Effect of Catecholate Binding. *J. Phys. Chem. B* **2006**, *110*, 9012−9021.
(60) Abate, S. Y.; Wu, W.-T.; Pola, S.; Tao, Y.-T. Compact TiO_2 Films with Sandwiched Ag Nanoparticles as Electron-Collecting Layer in Planar Type Perovskite SOlar Cells: Improvement in Efficiency and Stability. *RSC Adv.* **2018**, *8*, 7847−7854.
(61) Zuo, L.; Gu, Z.; Ye, T.; Fu, W.; Wu, G.; Li, H.; Chen, H. Enhanced Photovoltaic Performance of $CH_3NH_3PbI_3$ Perovskite Solar Cells through Interfacial Engineering Using Self-Assembling Monolayer. *J. Am. Chem. Soc.* **2015**, *137*, 2674−2679.
(62) Liu, Y.; Bag, M.; Renna, L. A.; Page, Z. A.; Kim, P.; Emrick, T.; Venkataraman, D.; Russell, T. P. Understanding Interface Engineering for High Performance Fullerene/Perovskite Planar Heterojunction Solar Cells. *Adv. Energy Mater.* **2016**, *6*, 1501606.
(63) Zhou, Y.; Fuentes-Hernandez, C.; Shim, J.; Meyer, J.; Giordano, A. J.; Li, H.; Winget, P.; Papadopoulos, T.; Cheun, H.; Kim, J.; Fenoll, M.; Dindar, A.; Haske, W.; Najafabadi, E.; Khan, T. M.; Sojoudi, H.; Barlow, S.; Graham, S.; Brédas, J.-L.; Marder, S. R.; Kahn, A.; Kippelen, B. A Universal Method to Produce Low−Work Function Electrodes for Organic Electronics. *Science* **2012**, *336*, 327−332.
(64) Courtright, B. A. E.; Jenekhe, S. A. Polyethylenimine Interfacial Layers in Inverted Organic Photovoltaic Devices: Effects of Ethoxylation and Molecular Weight on Efficiency and Temporal Stability. *ACS Appl. Mater. Interfaces* **2015**, *7*, 26167−26175.
(65) Yip, H.-L.; Hau, S. K.; Baek, N. S.; Ma, H.; Jen, A. K.-Y. Polymer Solar Cells That Use Self-Assembled-Monolayer-Modified ZnO/Metals as Cathodes. *Adv. Mater.* **2008**, *20*, 2376−2382.
(66) Srinivasan, S. *Fuel Cells*; Springer: US, 2006.
(67) Im, J.-H.; Lee, C.-R.; Lee, J.-W.; Park, S.-W.; Park, N.-G. 6.5% Efficient Perovskite Quantum-Dot-Sensitized Solar Cell. *Nanoscale* **2011**, *3*, 4088−4093.
(68) Heo, J. H.; Im, S. H.; Noh, J. H.; Mandal, T. N.; Lim, C.-S.; Chang, J. A.; Lee, Y. H.; Kim, H.-J.; Sarkar, A.; Nazeeruddin, M. K.; Grätzel, M.; Seok, S. I. Efficient Inorganic-Organic Hybrid Heterojunction Solar Cells Containing Perovskite Compound and Polymeric Hole Conductors. *Nat. Photonics* **2013**, *7*, 486−491.
(69) Shao, Y.; Xiao, Z.; Bi, C.; Yuan, Y.; Huang, J. Origin and Elimination of Photocurrent Hysteresis by Fullerene Passivation in $CH_3NH_3PbI_3$ Planar Heterojunction Solar Cells. *Nat. Commun.* **2014**, *5*, 5784.
(70) Sun, C.; Wu, Z.; Yip, H.-L.; Zhang, H.; Jiang, X.-F.; Xue, Q.; Hu, Z.; Hu, Z.; Shen, Y.; Wang, M.; Huang, F.; Cao, Y. Amino-Functionalized Conjugated Polymer as an Efficient Electron Transport Layer for High-Performance Planar-Heterojunction Perovskite Solar Cells. *Adv. Energy Mater.* **2016**, *6*, 1501534.
(71) Mir, W. J.; Swarnkar, A.; Nag, A. Postsynthesis Mn-doping in $CsPbI_3$ Nanocrystals to Stabilize the Black Perovskite Phase. *Nanoscale* **2019**, *11*, 4278−4286.
(72) Qiao, T.; Parobek, D.; Dong, Y.; Ha, E.; Son, D. H. Photoinduced Mn Doping in Cesium Lead Halide Perovskite Nanocrystals. *Nanoscale* **2019**, *11*, 5247−5253.
(73) Yang, H.; Fan, W.; Hills-Kimball, K.; Chen, O.; Wang, L.-Q. Introducing Manganese-Doped Lead Halide Perovskite Quantum Dots: A Simple Synthesis Illustrating Optoelectronic Properties of Semiconductors. *J. Chem. Educ.* **2019**, *96*, 2300−2307.
(74) Zuo, C.; Ding, L. An 80.11% FF Record Achieved for Perovskite Solar Cells by Using the NH_4Cl Additive. *Nanoscale* **2014**, *6*, 9935−9938.
(75) Niemann, R. G.; Kontos, A. G.; Palles, D.; Kamitsos, E. I.; Kaltzoglou, A.; Brivio, F.; Falaras, P.; Cameron, P. J. Halogen, Halogen Effects on Ordering and Bonding of $CH_3NH_3^+$ in $CH_3NH_3PbX_3$ (X = Cl, Br, I) Hybrid Perovskites: A Vibrational Spectroscopic Study. *J. Phys. Chem. C* **2016**, *120*, 2509−2519.
(76) Antoniadou, M.; Siranidi, E.; Vaenas, N.; Kontos, A. G.; Stathatos, E.; Falaras, P. Photovoltaic Performance and Stability of $CH_3NH_3PbI_{3-x}Clx$ Perovskites. *J. Surf. Interface Mater.* **2014**, *2*, 323−327.
(77) Barbe, J.; Kumar, V.; Newman, M. J.; Lee, H. K. H.; Jain, S. M.; Chen, H.; Charbonneau, C.; Rodenburg, C.; Tsoi, W. C. Dark Electrical Bias Effects on Moisture-Induced Degradation in Inverted Lead Halide Perovskite Solar Cells Measured by Using Advanced Chemical Probes. *Sust. Energy Fuels* **2018**, *2*, 905−914.
(78) Bella, F.; Griffini, G.; Correa-Baena, J.-P.; Saracco, G.; Grätzel, M.; Hagfeldt, A.; Turri, S.; Gerbaldi, C. Improving Efficiency and Stability of perovskite solar Cells with Photocurable Fluoropolymers. *Science* **2016**, *354*, 203−206.
(79) Snaith, H. J.; Hacke, P. Enabling Reliability Assessments of Pre-commercial Perovskite Photovoltaics with Lessons Learned from Industrial Standards. *Nat. Energy* **2018**, *3*, 459−465.
(80) Gujar, T. P.; Thelakkat, M. Highly Reproducible and Efficient Perovskite Solar Cells with Extraordinary Stability from Robust $CH_3NH_3PbI_3$: Towards Large-Area Devices. *Energy Technol.* **2016**, *3*, 449−457.
(81) Conings, B.; Drijkoningen, J.; Gauquelin, N.; Babayigit, A.; D'Haen, J.; Olieslaeger, L.; Ethirajan, A.; Verbeeck, J.; Manca, J.; Mosconi, E.; De Angelis, F.; Boyen, H.-G. Intrinsic Thermal Instability of Methylammonium Lead Trihalide Perovskite. *Adv. Energy Mater.* **2015**, *5*, 1500477.

https://dx.doi.org/10.1021/acsaem.0c00710
ACS Appl. Energy Mater. 2020, 3, 7353−7363